Exchange current model for $(La_{0.8}Sr_{0.2})_{0.95}MnO_3$ (LSM) porous cathode for solid oxide fuel cells

Kota Miyoshi[a] (Corresponding author), Takuma Miyamae[a], Hiroshi Iwai[a], Motohiro Saito[a], Masashi Kishimoto[a], and Hideo Yoshida[a]

[a] Department of Aeronautics and Astronautics, Kyoto University, Kyoto, 615-8540, Japan

Phone: +81 75 383 3652

Email address: miyoshikota@gmail.com

Abstract

In this paper, we propose an empirical formula for $i_{0,\mathrm{TPB}}$, the exchange current density per unit triple-phase boundary (TPB) length, for porous lanthanum strontium manganite (LSM) cathodes of solid oxide fuel cells (SOFCs); the evaluation of $i_{0,\mathrm{TPB}}$ is of crucial importance in numerical simulations of electrodes based on reconstructed microstructures obtained by a dual beam focused ion beam scanning electron microscopy (FIB-SEM) and tomography techniques. To derive a widely applicable empirical formula for $i_{0,\mathrm{TPB}}$,

electrochemical measurements of porous LSM cathodes are conducted under various oxygen partial pressures (0.05–0.25 atm) and temperatures (800–950 °C). By comparing the derived formula with that derived from a thin and dense patterned LSM electrode used in previous studies, it is found that at an air temperature of 800 °C, $i_{0,\mathrm{TPB}}$ derived from a porous LSM cathode is approximately 40% smaller than that for the patterned electrode. This can be attributed to the fact that the electrochemical reaction in thin and dense electrodes can occur not only at the TPBs but also at the LSM surface owing to the non-negligible ionic conductivity of LSM. The derived formula is also applied to a three-dimensional numerical simulation to confirm its validity.

Keywords: Solid oxide fuel cells, LSM, Cathode, FIB-SEM, Exchange current

1. Introduction

The porous microstructure of SOFC electrodes is considered to have a significant effect on their power generation performance because the electrochemical reaction within the electrodes requires the sufficient transport of gas species, electrons and oxide ions through the complex multiphase porous structure. The recent development and improvement of 3D imaging techniques, such as focused ion beam scanning electron microscopy (FIB-SEM) and X-ray computed tomography, have enabled us to obtain detailed electrode microstructures in three dimensions [1-3], which are useful for obtaining insights into microstructure–performance relationships.

Three-dimensional datasets of porous electrodes can also be applied to the numerical analysis of electrode electrochemical performance [4-9], where the rate equations for the electrochemical reactions are among the most essential factors that determine the accuracy of the simulation. Rate equations are often expressed by Butler–Volmer-like forms that include the density of the reaction sites, i.e., triple-phase boundaries (TPBs) or double-phase boundaries (DPBs), and the exchange current density per unit reaction site area/length. The TPB density is considered important for conventional cermet materials, such as Ni-YSZ (yttria-stabilized zirconia) and LSM-YSZ (lanthanum strontium manganite/yttria-stabilized

zirconia), while the DPB density is considered important for mixed ionic-electronic conductors, such as doped ceria and LSCF (lanthanum strontium cobalt ferrite). For conventional cermet electrodes, the exchange current density per unit TPB length ($i_{0,\mathrm{TPB}}$) has been measured from experiments using thin and dense patterned electrodes because of the advantage that the TPB length is well defined from their geometry.

In the case of LSM-YSZ cathodes, Radhakrishnan et al. [10] conducted electrochemical measurements at various temperatures (650–800 °C) and oxygen partial pressures (0.01–1 atm) using patterned LSM cathodes with a thickness of 500 nm. Konno et al. [11] derived a power-law-type formula for $i_{0,\mathrm{TPB}}$ based on the experimental results of Radhakrishnan et al. This empirical formula can be applied to numerical simulations. However, in our preliminary study, a large discrepancy was observed between numerical simulation results for a LSM cathode using this empirical formula and experimental results. One of the possible reasons for this is that the small ionic conductivity of LSM can expand the reaction region from TPBs to DPBs (LSM-pore boundaries) in a thin and dense patterned electrode. For instance, Brichzin et al. [12] conducted experiments on patterned electrodes with thicknesses of 100 and 250 nm and found that the thickness of the patterned LSM electrodes affected the activation overpotential. Furthermore, Horita et al. [13] observed oxygen ion diffusion inside

a patterned LSM cathode with a thickness of 490 nm by secondary ion mass spectrometry and reported that the oxide ions were transferred through the thin and dense LSM. Yasuda et al. [14] also reported that under an oxygen partial pressure of 100 torr (ca. 0.13 atm), oxygen ions could penetrate through a thin and dense LSM. These studies [12-14] show that charge transfer can occur at DPBs in thin patterned electrodes. This is also supported by a report of Gong et al. [15], according to which the DPB reaction in LSM cathodes can only be negligible at a distance exceeding about 1 μm from the LSM/electrolyte interface at 800 °C. Most of the DPBs in the thin patterned LSM cathodes used in Refs. [12-14] existed within 500 nm from the LSM/electrolyte interface, and therefore they are expected to be electrochemically active. This makes it difficult to evaluate $i_{0,\mathrm{TPB}}$ from experiments using the thin and dense patterned LSM cathodes. Therefore, an empirical formula for $i_{0,\mathrm{TPB}}$ in LSM cathodes should be derived from actual porous LSM cathodes to minimize the contribution of the DPBs to the electrochemical activity of the electrode. Although the TPB length cannot be easily measured in actual porous electrodes, FIB-SEM enables us to evaluate the TPB density even in complex microstructures with a resolution of 10 nm order.

In this study, we conduct electrochemical measurements of porous LSM electrodes (particle diameter: ca. 3 μm) to derive an empirical formula for $i_{0,\mathrm{TPB}}$ over a range of

temperatures (800–950 °C) and oxygen partial pressures (0.05–0.25 atm). After the experiments, the porous LSM cathode is imaged by FIB-SEM and the TPB density is evaluated. From these experimental datasets, we estimate $i_{0,\mathrm{TPB}}$ values, from which an empirical formula for $i_{0,\mathrm{TPB}}$ derived from porous LSM cathodes is proposed and compared with a formula derived from patterned LSM cathodes [11]. The formula is then adopted in a 3D numerical simulation of an LSM-YSZ composite cathode and the results are compared with experimental results to confirm the validity of the formula derived in this study.

2. Derivation of the exchange current density model

The relationship between the charge transfer current density (i_{ct} [A m^{-2}]) and the activation overpotential (η_{act} [V]) is often described by Butler–Volmer-like forms [16] using the TPB density (l_{TPB} [m^{-1}]) and the exchange current density per unit TPB length ($i_{0,\mathrm{TPB}}$ [A m^{-1}]):

$$i_{\mathrm{ct}} = i_{0,\mathrm{TPB}} l_{\mathrm{TPB}} \left\{ \exp\left(\frac{2F}{RT}\eta_{\mathrm{act}}\right) - \exp\left(-\frac{2F}{RT}\eta_{\mathrm{act}}\right) \right\} \quad (1)$$

where T is the temperature, F is the Faraday constantant and R is the gas constant. To experimentally estimate $i_{0,\mathrm{TPB}}$, the following are required: (i) the relationship between the activation overpotential and the charge transfer current density and (ii) the total TPB length in the LSM cathodes. Therefore, we first conducted electrochemical measurements using porous LSM cathodes then performed a 3D analysis of the cathode microstructure by FIB-SEM. From the electrochemical and microstructural analyses, an empirical formula for $i_{0,\mathrm{TPB}}$ was obtained.

2.1. Experimental

2.1.1. Electrochemical characterization

The electrodes examined in this study were the LSM ($(La_{0.8}Sr_{0.2})_{0.95}MnO_3$) cathodes of a Ni-YSZ/YSZ/LSM button cell. The anode material, NiO-YSZ (50 vol.% Ni-50 vol.% YSZ), was mixed with polyethylene glycol, screen-printed on a YSZ disk electrolyte (TOSOH Co., 24 mm in diameter, 500 μm in thickness) and sintered at 1400 °C for 5 h. LSM paste consisted of LSM powder and Terpineol (LSM20-I, NexTech materials) was also screen-printed on the other side of the electrolyte and sintered at 1150 °C for 5 h. The thickness of the LSM cathode and the Ni-YSZ anode was ca. 18-20 μm and ca. 30 μm, respectively. The electrode areas for both electrodes were ca. 0.785 cm^2. As a reference electrode, platinum wire was attached around the side edge of the disk electrolyte. An oxygen-nitrogen mixture and 3% humidified hydrogen were supplied with a flow rate of 100 mL min^{-1} to the cathode and anode, respectively. The experimental set-up was the same as that used by Kishimoto et al. [8]. The cathode performance, such as the activation overpotential, was obtained by electrochemical impedance spectroscopy (EIS) and current–voltage (*I–V*) measurement at various temperatures (800, 850 and 950 °C) and oxygen concentrations (5, 10, 21 and 25%) using a Solartron 1287A electrochemical interface. At

900 °C, the oxygen concentration was varied from 5% to 25% at intervals of 2%. From our preliminary experiments with this button cell, it was confirmed that the inductor element in the cells is ca. 80 nH, and does not significantly alter the Nyquist plot. The ohmic resistance was estimated from the high-frequency intercept of the Nyquist plot under the OCV condition, and total cathode overpotential was measured by the *I–V* measurement. The activation overpotential characteristics were obtained by subtracting the ohmic loss from the total cathode overpotential.

2.1.2. FIB-SEM imaging

After the power generation experiments, the cathodes were cooled to room temperature in air (21% O_2-79 % N_2) and then impregnated with epoxy resin (Epofix, Struers) under a vacuum condition so that the pores could be distinguished from the solid phases in SEM imaging. The 3D microstructure of the sample cathodes was obtained by FIB-SEM (NVision 40, Zeiss). The procedure used for FIB-SEM imaging was similar to that employed by Kishimoto et al. [4]. After the SEM imaging of an exposed cross-sectional surface, the surface was slightly milled by FIB so that a new surface was exposed for the next SEM imaging. By repeated FIB milling and SEM imaging, a series of 2D SEM images was

obtained. During the SEM imaging, an in-lens secondary electron detector was used with an acceleration voltage of 1.5 kV. The series of images was aligned using the least-squares method. Phase segmentation was conducted on the basis of the brightness, which was followed by manual correction. Commercial image processing software (AVIZO, FEI) was used for the alignment, phase segmentation and 3D reconstruction of the cathode microstructure.

2.1.3. Experimental results

Figure 1 shows the 3D reconstructed image of the LSM microstructure and TPB distribution. In the porous LSM cathode, TPBs only exist at the electrode-electrolyte interface. From this reconstructed structure, the TPB density after the experiment was estimated to be 1.55 μm^{-1}. Note that the TPB density was evaluated by dividing the total TPB length by the apparent surface area $12.1 \times 25.0\ \mu m^2$ of the LSM cathode. Table 1 summarizes the microstructural parameters. Details of the quantification techniques can be found elsewhere [3].

To derive of an exchange current density model, we assumed that (i) the charge transfer reaction occurs only at TPBs and (ii) the concentration overpotential is negligible at a low

current density. Therefore, $i_{0,\mathrm{TPB}}$ can be estimated experimentally by substituting the charge transfer current density, activation overpotential and TPB density into Eq. 1. In this study, a current density of 10 mA cm^{-2} and the corresponding activation overpotential were used for i_{ct} and η_{act}, respectively. Figure 2(a) shows the experimentally estimated $i_{0,\mathrm{TPB}}$ as a function of oxygen concentration at 900 °C and Fig. 2(b) shows it as a function of temperature in the case of 21% O_2. A higher oxygen concentration and temperature lead to a higher $i_{0,\mathrm{TPB}}$. The derivation of $i_{0,\mathrm{TPB}}$ will be presented in the next section.

2.2.Derivation of the formula for $i_{0,\mathrm{TPB}}$

We adopted the following power-law formula for $i_{0,\mathrm{TPB}}$ by considering its dependence on the temperature and oxygen partial pressure: $i_{0,\mathrm{TPB}} = A{P_{\mathrm{O}_2}}^{a} \exp\left(\frac{-E}{RT}\right)$, where P_{O_2} [Pa] is the oxygen partial pressure, and A, a and E are fitted to experimental data. The fitting method was similar to that employed by Brus et al. [17]. Equation 1 can be rewritten using a reaction constant k as

$$i_{\mathrm{ct}} = k{P_{\mathrm{O}_2}}^{a} l_{\mathrm{TPB}} \left\{\exp\left(\frac{2F}{RT}\eta_{\mathrm{act}}\right) - \exp\left(-\frac{2F}{RT}\eta_{\mathrm{act}}\right)\right\} \quad (2)$$

$$k = A \exp\frac{-E}{RT} \quad (3)$$

According to Eqs. 2 and 3, k has to be independent of the oxygen partial pressure at a given temperature. From the series of measurements conducted at 900 °C with various oxygen partial pressures, a set of k values can be obtained when a certain value is assumed for the exponent a. The exponent a can be determined so that the obtained set of k values becomes identical. In reality, however, the values of k never become identical, regardless of the value assumed for a, owing to inevitable experimental errors. Therefore, we defined the relative standard deviation of k as a function of a as follows and found the value for a that minimized it:

$$\sigma(a) = \frac{1}{\bar{k}(a)}\sqrt{\frac{1}{N}\sum_{i=1}^{N}[\,k_i(a) - \bar{k}(a)]^2}, \quad \bar{k}(a) = \frac{1}{N}\sum_{i=1}^{N} k_i\,(a) \tag{4}$$

where $k_i(a)$ is the value of k for each oxygen partial pressure and a given exponent a, and $\bar{k}(a)$ is their average. Figure 3(a) shows the dependence of $\sigma(a)$ on a, from which a was determined to be 0.376.

A and E were estimated from the experiments carried out at different temperatures with 21% O_2. The obtained value of a was also used. Equation 3 can be rewritten in the

Arrhenius form

$$\ln\ k = \ln\ A - \frac{E}{RT} \tag{5}$$

Figure 3(b) shows an Arrhenius plot of the experimental results and the fitted linear line obtained by the least-squares method. The values of A and E were then evaluated from the intercept and the slope of the line to be 2.14×10^5 and -2.43×10^5, respectively.

From the above analysis, we derived the following empirical formula for $i_{0,\mathrm{TPB}}$ for LSM cathodes:

$$i_{0,\mathrm{TPB}} = 2.14 \times 10^5 P_{\mathrm{O}_2}^{0.376} \exp\left(\frac{-2.43\times10^5}{RT}\right) \tag{6}$$

Since the contribution of the DPBs is minimal in this empirical formula derived from the actual porous LSM, the $i_{0,\mathrm{TPB}}$ values are expected to be smaller than those derived from patterned LSM. The empirical formula for $i_{0,\mathrm{TPB}}$ derived from patterned LSM cathodes is [10, 11]

$$i_{0,\mathrm{TPB}} = 1.10 P_{\mathrm{O_2}}^{0.5} \exp\left(\frac{-1.37\times10^{5}}{RT}\right) \quad (7)$$

The difference between $i_{0,\mathrm{TPB}}$ for the actual porous LSM (Eq. 6) and the patterned LSM (Eq. 7) is shown in Fig. 4. It was found that $i_{0,\mathrm{TPB}}$ derived from the porous LSM cathode was smaller than that derived from the patterned LSM cathode over the entire range of oxygen partial pressures at 800 °C, for example it was approximately 40% smaller in air. This discrepancy can be attributed to the DPB effects. In the patterned LSM cathode, the charge transfer reaction can occur at DPBs because of the small ionic conductivity of LSM, and the empirical formula contains such effects, resulting in the overestimation of $i_{0,\mathrm{TPB}}$.

3. Validation of the formula for $i_{0,\mathrm{TPB}}$

To confirm the validity of the empirical formula for $i_{0,\mathrm{TPB}}$, we conducted (1) electrochemical measurements of an LSM-YSZ composite cathode to obtain $i-\eta_{\mathrm{act}}$ characteristics and (2) FIB-SEM imaging of the cathode after the experiment to obtain its microstructure. Note that LSM-YSZ composite cathode was made in the same method as described in section 2.1.1 using LSM-YSZ paste (50 wt.% LSM-50 wt.% YSZ, LSMYSZ-I, NexTech materials). Using the obtained 3D microstructure and the $i_{0,\mathrm{TPB}}$ model derived in this study, a 3D numerical simulation of the LSM-YSZ composite cathode is conducted. The simulation results were compared with the experimentally obtained $i-\eta_{\mathrm{act}}$ characteristics.

3.1. Numerical model

The simulation was based on the finite volume method (FVM), where the conservation of electrons, ions and gas species was considered. The electrochemical reaction was assumed to take place only at the TPBs. Figure 5 shows the calculation domain. The *x* axis corresponds to the depth direction of the cathode. Table 2 summarizes the microstructural parameters of the LSM-YSZ composite cathode. In this microstructure, TPBs are distributed within the entire cathode structure. Although the thickness of the LSM-YSZ layer was

approximately 20 μm, the reconstructed microstructure only had a thickness of 14 μm. Therefore, the whole cathode structure obtained by FIB-SEM was mirror-symmetrically extended in the *x* direction and cut so as to attain an equivalent thickness of 20 μm. The temperature was assumed to be constant and uniform in the cathode.

In this model, the local transport coefficients in each grid $\Gamma_i^{\mathrm{eff,local}}$ are evaluated as

$$\Gamma_i^{\mathrm{eff,local}} = V_i^{\mathrm{local}} \Gamma_i^{\mathrm{bulk}} \tag{8}$$

where V_i is the volume fraction of phase i in the grid. Details of the model can be found elsewhere [4, 5].

3.1.1. Governing equations for gas transport

The conservation of gas species i is given in terms of the molar flux N_i and source term s_i as

$$\nabla \cdot N_i = s_i \tag{9}$$

The dusty-gas model was used to simulate gas diffusion in porous cathodes. We assumed that the total pressure gradient was negligibly small. Then, the dusty-gas model can be written as

$$\frac{N_i}{D_{i,\mathrm{K}}^{\mathrm{eff}}} + \sum_{j=1,j\neq i}^{n} \frac{X_j N_i - X_i N_j}{D_{ij}^{\mathrm{eff}}} = -\frac{P_{\mathrm{t}}}{RT} \nabla X_i \tag{10}$$

where X_i, P_i and N_i are the molar fraction, partial pressure and molar flux of gas species i, P_{t} is the total pressure, and $D_{i,\mathrm{K}}^{\mathrm{eff}}$ and D_{ij}^{eff} are the effective Knudsen diffusion coefficients and the effective binary diffusion coefficients, respectively.

The source term s_i is given by i_{ct}, the charge transfer current density at TPBs as

$$s_{\mathrm{O_2}} = \frac{i_{\mathrm{ct}}}{4F}, \quad s_{\mathrm{N_2}} = 0 \tag{11}$$

3.1.2. Governing equations for electron and ion transport

The conservation of electrons and ions is expressed in terms of the electrochemical potentials as

$$\nabla \cdot \left(\frac{\sigma_{e^-}^{\text{eff}}}{F} \nabla \tilde{\mu}_{e^-} \right) = -i_{\text{ct}}, \quad \nabla \cdot \left(\frac{\sigma_{o^{2-}}^{\text{eff}}}{2F} \nabla \tilde{\mu}_{o^{2-}} \right) = i_{\text{ct}} \tag{12}$$

where $\tilde{\mu}_{e^-}$ and $\tilde{\mu}_{o^{2-}}$ are the electrochemical potentials of electrons and oxide ions, and $\sigma_{e^-}^{\text{eff}}$ and $\sigma_{o^{2-}}^{\text{eff}}$ are the effective electron and ion conductivities, respectively. The bulk conductivities are given as follows:

LSM phase [18, 19]

$$\sigma_{e^-} = \frac{4.2\times10^7}{T} \exp\left(\frac{-1200}{T}\right) \tag{13}$$

$$\sigma_{o^{2-}} = 4.0 \times 10^{-6} \tag{14}$$

YSZ phase [20, 21]

$$\sigma_{e^-} = \max \begin{pmatrix} 1.31 \times 10^9 \exp\left(\frac{-4.52\times10^4}{T}\right) \left(\frac{P_{O_2,\text{YSZ}}}{101325}\right)^{-\frac{1}{4}}, \\ 2.35 \times 10^4 \exp\left(\frac{-1.94\times10^4}{T}\right) \left(\frac{P_{O_2,\text{YSZ}}}{101325}\right)^{\frac{1}{4}} \end{pmatrix} \tag{15}$$

$$\sigma_{o^{2-}} = 3.40 \times 10^{-4} \exp\left(\frac{-10350}{T}\right) \tag{16}$$

where $P_{O_2,\text{YSZ}}$ is the local partial pressure of oxygen in the YSZ phase and can be estimated

from the electrochemical potentials as follows by assuming local thermodynamic equilibrium:

$$\tilde{\mu}_{\mathrm{o}^{2-}} - 2\tilde{\mu}_{\mathrm{e}^{-}} = \frac{1}{2}RT \ln\left(\frac{P_{\mathrm{O}_2,\mathrm{YSZ}}}{10^5}\right) \tag{17}$$

$$P_{\mathrm{O}_2,\mathrm{YSZ}} = 10^5 \exp\left(\frac{2(\tilde{\mu}_{\mathrm{o}^{2-}} - 2\tilde{\mu}_{\mathrm{e}^{-}})}{RT}\right) \tag{18}$$

3.1.3. Electrochemical reaction

The charge transfer current density i_{ct} for oxygen reduction in the cathode can be expressed by the Butler–Volmer-like equation (Eq. 1). Equations 6 and 7 were used for the $i_{0,\mathrm{TPB}}$ formula for comparison.

The activation overpotential η_{act} and concentration overpotential η_{con} are expressed as

$$\eta_{\mathrm{act}} = -\frac{1}{2F}\left(-\tilde{\mu}_{\mathrm{o}^{2-}} + 2\tilde{\mu}_{\mathrm{e}^{-}} + \frac{1}{2}RT \ln\left(\frac{P_{\mathrm{O}_2}^{\mathrm{in}}}{10^5}\right)\right) - \eta_{\mathrm{con}} \tag{19}$$

$$\eta_{\mathrm{con}} = \frac{1}{4F}RT\ln\left(\frac{P_{\mathrm{O}_2}}{P_{\mathrm{O}_2}^{\mathrm{in}}}\right) \tag{20}$$

3.1.4. Boundary conditions

The boundary conditions used in the calculation are summarized in Table 3. The gas composition was constant on the cathode surface to represent the supplied gas composition. To determine the cathode overpotential, the electrochemical potential of electrons at the cathode surface and that of oxide ions at the cathode-electrolyte interface were appropriately set. Also, no flux conditions were set on the cathode surface for the electrochemical potential of oxide ions and on the cathode-electrolyte interface for the gas components and the electrochemical potential of electrons.

3.2. Results and discussion

Figure 6 shows the $i-\eta_{\mathrm{act}}$ characteristics at 800 °C obtained experimentally and numerically. The simulation results in Fig. 6(a) were calculated using $i_{0,\mathrm{TPB}}$ derived from the porous LSM, while those in Fig. 6(b) were calculated using $i_{0,\mathrm{TPB}}$ derived from the patterned LSM. The temperature was chosen to be 800 °C because it is within the range covered by both Eqs. 6 and 7. The simulation results obtained using Eq. 6 show better agreement with the experimental results at 800 °C than those obtained using Eq. 7. In this study, we derived Eq. 6 from an actual porous LSM cathode to minimize the effect of the

reaction at the DPBs. Therefore, this good agreement indicates that the reaction at the DPBs in the LSM-YSZ composite cathode is insignificant compared with that at the TPBs and that Eq. 6 is more accurate than Eq. 7 for describing the reaction rate at the TPBs even in the LSM-YSZ composite cathode.

Figure 7 shows the simulation results obtained using Eq. 6 and the experimental results under an oxygen concentration of 21%. The results of the simulation using Eq. 6 are in good agreement with the experimental results not only at 800 °C but also at 950 °C.

Figure 8 shows the 1D average charge transfer current density as a function of the cathode depth (cathode surface at $x = 0$) at 850 °C. The active thickness was found to be ca. 10 μm at 850 °C under all conditions. This result is consistent with the report by Juhl et al. [22], where the active thickness in an LSM-YSZ composite cathode was experimentally evaluated using an LSM-YSZ composite cathode by varying the thickness of the cathode at 850 °C. They found that the cathode overpotential did not increase until the cathode thickness was decreased to below ca. 10 μm, from which they determined the active thickness in the LSM-YSZ cathode to be ca. 10 μm. This supports the validity of our empirical formula.

4. Conclusions

In this study, an empirical formula for the exchange current density per unit TPB length in a lanthanum strontium manganite cathode for SOFCs was derived through electrochemical measurement of a porous LSM cathode and microstructural analysis by FIB-SEM. From the electrochemical measurement, the dependence of the activation overpotential on the electrode temperature and oxygen partial pressure was obtained, which was used to calculate the exchange current density within the cathode. Combined with the quantified TPB density obtained from the reconstructed datasets, the exchange current density per unit TPB length was evaluated and then fitted to a power-law formula containing the temperature and oxygen partial pressure. The values of $i_{0,\mathrm{TPB}}$ obtained in this study were found to be smaller than those estimated from a patterned electrode at oxygen partial pressures in the range of 5–25% at 800 °C, for example, $i_{0,\mathrm{TPB}}$ was approximately 40% smaller in air. One possible reason for this is that the value of $i_{0,\mathrm{TPB}}$ derived from the thin and dense patterned LSM included the effect of the reaction at LSM-pore double-phase boundaries.

To confirm the validity of the formula for $i_{0,\mathrm{TPB}}$ derived from the porous LSM cathode, it was applied to a three-dimensional numerical model of a LSM-YSZ cathode. The formula derived in this study yielded better agreement between the simulation and experimental result

than that derived from a patterned LSM cathode in the literature. The proposed formula is expected to be valid for porous LSM and LSM-YSZ composite cathodes under oxygen partial pressures of 0.05–0.25 atm and temperatures of 800–950 °C.

Acknowledgments

This work was supported by the New Energy and Industrial Technology Development Organization (NEDO) under the Development of System and Elemental Technology for Solid Oxide Fuel Cell (SOFC) Project and by a Grant-in-Aid for JSPS Fellows.

References

[1] J.R. Wilson, W. Kobsiriphat, R. Mendoza, H.-Y. Chen, J.M. Hiller, D.J. Miller, K. Thornton, P.W. Voorhees, S.B. Adler, S.A. Barnett, Three-dimensional reconstruction of a solid-oxide fuel-cell anode, Nature Materials, 5 (2006) 541.

[2] H. Iwai, N. Shikazono, T. Matsui, H. Teshima, M. Kishimoto, R. Kishida, D. Hayashi, K. Matsuzaki, D. Kanno, M. Saito, H. Muroyama, K. Eguchi, N. Kasagi, H. Yoshida, Quantification of SOFC anode microstructure based on dual beam FIB-SEM technique, Journal of Power Sources, 195 (2010) 955.

[3] M. Kishimoto, H. Iwai, M. Saito, H. Yoshida, Quantitative evaluation of solid oxide fuel cell porous anode microstructure based on focused ion beam and scanning electron microscope technique and prediction of anode overpotentials, Journal of Power Sources, 196 (2011) 4555.

[4] M. Kishimoto, H. Iwai, M. Saito, H. Yoshida, Three-dimensional simulation of SOFC anode polarization characteristics based on sub-grid scale modeling of microstructure, Journal of the Electrochemical Society, 159 (2012) B315.

[5] M. Kishimoto, H. Iwai, K. Miyawaki, M. Saito, H. Yoshida, Improvement of the sub-grid-scale model designed for 3D numerical simulation of solid oxide fuel cell electrodes using an adaptive power index, Journal of Power Sources, 223 (2013) 268.

[6] K. Matsuzaki, N. Shikazono, N. Kasagi, Three-dimensional numerical analysis of mixed ionic and electronic conducting cathode reconstructed by focused ion beam scanning electron microscope, Journal of Power Sources, 196 (2011) 3073.

[7] T. Carraro, J. Joos, B. Rüger, A. Weber, E. Ivers-Tiffee, 3D finite element model for reconstructed mixed-conducting cathodes: I. Performance quantification, Electrochimica Acta, 77 (2012) 315.

[8] M. Kishimoto, K. Miyawaki, H. Iwai, M. Saito, H. Yoshida, Effect of composition ratio of Ni-YSZ anode on distribution of effective three-phase boundary and power generation performance, Fuel Cells, 13 (2013) 476.

[9] D. Kanno, N. Shikazono, N. Takagi, K. Matsuzaki, N. Kasagi, Evaluation of SOFC anode polarization simulation using three-dimensional microstructures reconstructed by FIB tomography, Electrochimica Acta, 56 (2011) 4015.

[10] R. Radhakrishnan, A.V. Virkar, S.C. Singhal, Estimation of charge-transfer resistivity of $La_{0.8}Sr_{0.2}MnO_3$ cathode on $Y_{0.16}Zr_{0.84}O_2$ electrolyte using patterned electrodes, Journal of the Electrochemical Society, 152 (2005) A210.

[11] A. Konno, H. Iwai, M. Saito, H. Yoshida, A corrugated mesoscale structure on electrode–electrolyte interface for enhancing cell performance in anode-supported SOFC, Journal of Power Sources, 196 (2011) 7442.

[12] V. Brichzin, J. Fleig, H.-U. Habermeier, G. Cristiani, J. Maier, The geometry dependence of the polarization resistance of Sr-doped $LaMnO_3$ microelectrodes on yttria-stabilized zirconia, Solid State Ionics, 152–153 (2002) 499.

[13] T. Horita, K. Yamaji, M. Ishikawa, N. Sakai, H. Yokokawa, T. Kawada, T. Kato, Active sites imaging for oxygen reduction at the $La_{0.9}Sr_{0.1}MnO_{3-x}$ /yttria-stabilized

zirconia interface by secondary-ion mass spectrometry, Journal of the Electrochemical Society, 145 (1998) 3196.

[14] I. Yasuda, K. Ogasawara, M. Hishinuma, T. Kawada, Oxygen tracer diffusion coefficient of LSM, Solid State ionics, 86-88 (1996) 1197.

[15] M. Gong, R.S. Gemmen, X. Liu, Modeling of oxygen reduction mechanism for 3PB and 2PB pathways at solid oxide fuel cell cathode from multi-step charge transfer, Journal of Power Sources, 201 (2012) 204.

[16] R. Suwanwarangkul, E. Croiset, E. Entchev, S. Charojrochkul, M.D. Pritzker, M.W. Fowler, P.L. Douglas, S. Chewathanakup, H. Mahaudom, Experimental and modeling study of solid oxide fuel cell operating with syngas fuel, Journal of Power Sources, 161 (2006) 308.

[17] G. Brus, Y. Komatsu, S. Kimijima, An analysis of biogas reforming process on Ni/YSZ and Ni/SDC catalysts, International Journal of Thermodynamics, 15 (2012) 43.

[18] J.R. Ferguson, J.M. Fiard, R. Herbin, Three-dimensional numerical simulation for various geometries of solid oxide fuel cells, Journal of Power Sources. 58 (1996) 109.

[19] Y. Ji, J. Kilner, M. Carolan, Electrical properties and oxygen diffusion in yttria-stabilised zirconia (YSZ)–LaSrMnO (LSM) composites, Solid State Ionics, 176 (2005) 937.

[20] J.H. Park, R.N. Blumenthal, Electronic transport in 8 mole percent Y_2O_3-ZrO_2, Journal of the Electrochemical Society, 136 (1989) 2867.

[21] N.F. Bessette II, W.J. Wepfer, J. Winnick, A mathematical model of a solid oxide fuel cell, Journal of the Electrochemical Society, 142 (1995) 3792.

[22] M. Juhl, S. Primdahl, C. Manon, M. Mogensen, Performance/structure correlation for composite SOFC cathodes, Journal of Power Sources, 61 (1996) 173.

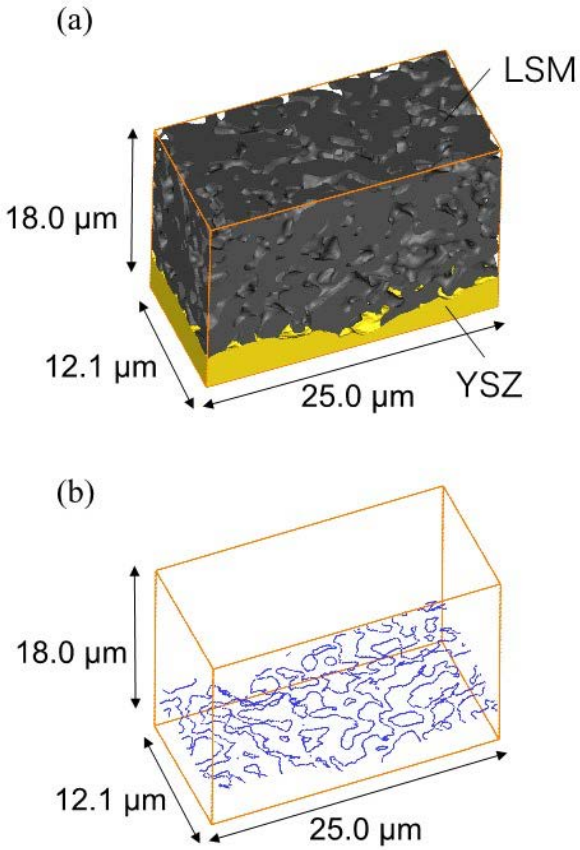

Fig. 1. Three-dimensional reconstructed image of (a) LSM microstructure and (b) TPB lines.

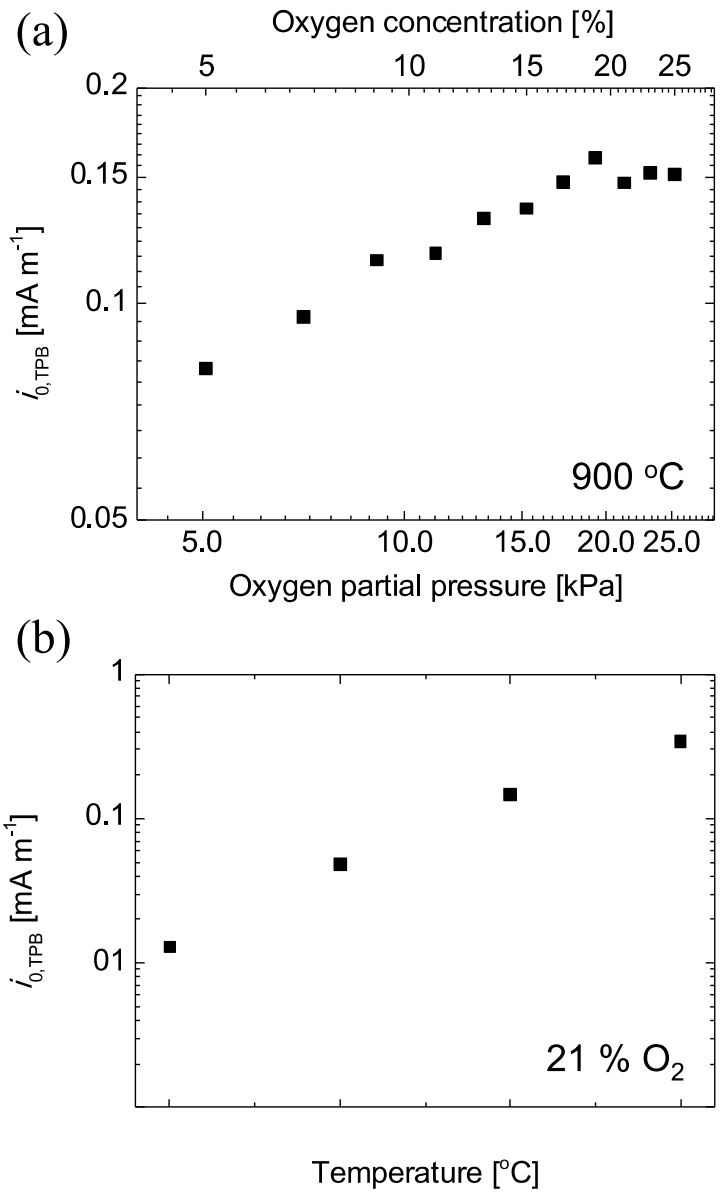

Fig. 2. Dependence of $\boldsymbol{i_{0,TPB}}$ on (a) oxygen concentration and (b) temperature.

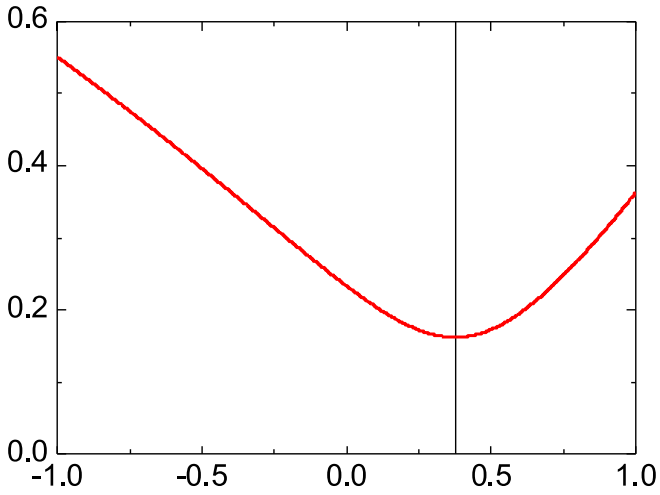

Fig. 3. (a) Relative standard deviation of the reaction constant $\boldsymbol{k}$ as a function of the exponent $\boldsymbol{a}$. (b) Arrhenius plot of the experimental results in the case of 21% oxygen.

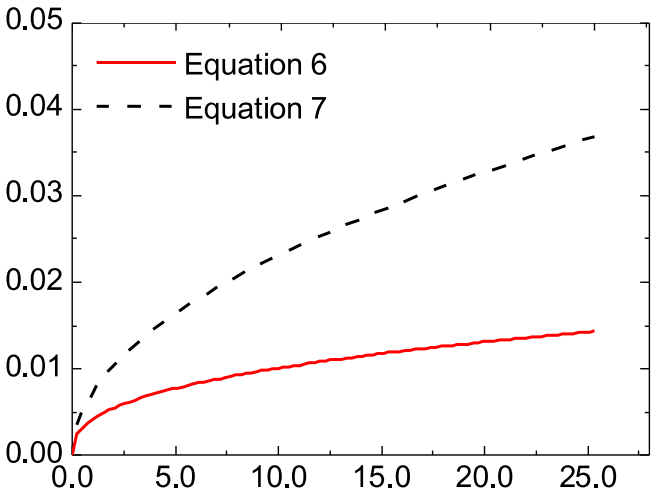

Fig. 4. $\boldsymbol{i_{0,\mathrm{TPB}}}$ estimated from Eq. 6 and Eq. 7 at 800 °C.

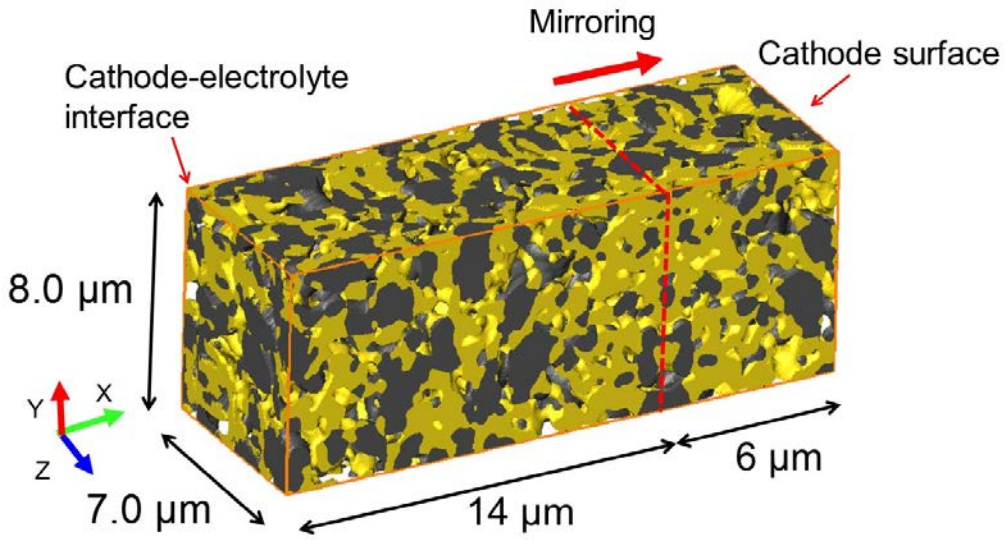

Fig. 5. Calculation domain.

(a) Equation 6 (porous LSM)

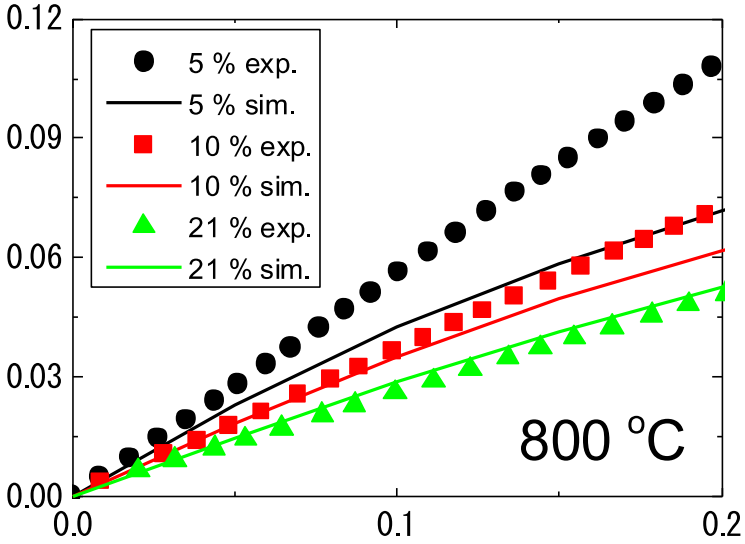

(b) Equation 7 (patterned LSM)

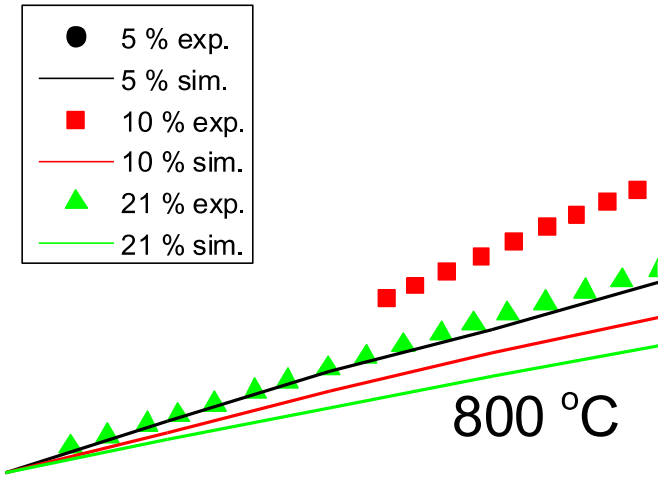

Fig. 6. Dependence of activation and concentration overpotentials on oxygen concentration as a function of current density. The simulation model uses (a) Eq. 6 and (b) Eq. 7 at 800 °C.

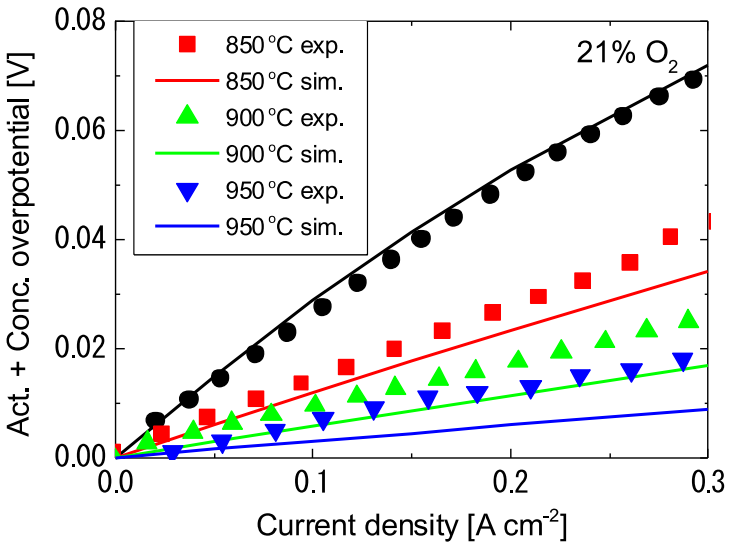

Fig. 7. Dependence of activation and concentration overpotentials on temperature as a function of current density. The simulation model uses Eq. 6 under an oxygen concentration of 21%.

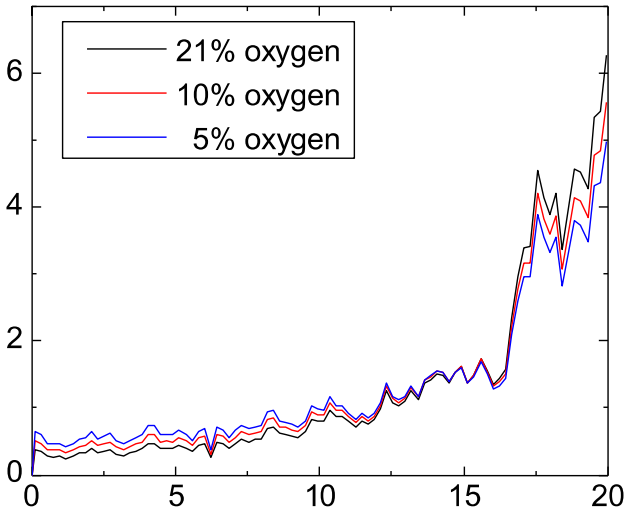

Fig. 8. 1D average charge transfer current as a function of cathode depth (cathode surface: $\boldsymbol{x = 0}$, cathode-electrolyte interface: $\boldsymbol{x = 20}$) at 850 °C.